Shape Sensitivities of 2D Airfoils for Broadband Noise Reduction Using the Adjoint Method and Semi-Analytical Models

Antoine Hajczak, Martin Buszyk

Shape sensitivities of 2D airfoils for broadband noise reduction using the adjoint method and semi-analytical models

Antoine Hajczak*
Sorbonne Université, CNRS, Institut Jean Le Rond d'Alembert, F-75005 Paris, France.

Martin Buszyk†
DAAA, ONERA, Institut Polytechnique de Paris, 92320, Châtillon, France

An adjoint-based methodology is developed and validated to numerically estimate the sensitivities of a semi-analytical model for computing the broadband noise associated to the interaction between a turbulent boundary layer and a two-dimensional airfoil trailing-edge. To this end, an acoustic objective function based on Amiet's theory in combination with a semi-empirical wall pressure spectrum model is proposed. The steady-state boundary layer integral quantities required by the semi-empirical model are obtained using Reynolds-Averaged Navier-Stokes simulations. After validation of this methodology on a NACA0012 airfoil, the model sensitivities are obtained numerically using algorithmic differentiation of computer programs. The sensitivities to camber and thickness, computed with the associated adjoint solver, are compared to finite differences evaluations on an asymmetric OAT15 airfoil at subsonic and transonic speeds. The results show that the model is most sensitive to camber and thickness variations close to the trailing-edge, especially at transonic speed. The adjoint method proves much more computationally efficient in obtaining the sensitivities than finite differences and offers perspectives for multi-disciplinary propeller blade shape optimization.

Nomenclature

$\mathbf{x} = (x, y, z)$	=	Cartesian coordinates	Λ	=	Objective function scaling factor
S_0	=	Convective distance	h	=	Finite differences step
ω	=	Pulsation	V_{ij}	=	Generic cell-center/cell-node value
L	=	Airfoil span	λ^T	=	Adjoint vector
$c = 2b$	=	Airfoil chord	S_{pp}	=	Far-field acoustic pressure PSD
$\mathbf{v} = (v_x, v_y, v_z)$	=	Fluid velocity	c_0	=	Speed of sound
E	=	Fluid total energy	Π_0	=	Wavenumber spectral density
ρ	=	Fluid density	K_y	=	Spanwise aerodynamic wavenumber
M	=	Mach number	k	=	Acoustic wavenumber
Re_c	=	Chord-based Reynolds number	$\mathcal{L}$	=	Airfoil transfer function
n	=	Number of shape parameters	l_y	=	Coherence length
$\alpha_{i,1\leq i\leq n}$	=	Shape parameters	U_c	=	Boundary layer convection velocity
$\mathcal{J}$	=	Acoustic objective function	U_e	=	Boundary layer external velocity
X	=	Volumic CFD grid	Φ_{pp}	=	Wall-pressure PSD
$W = (\rho, \rho v_x, \rho v_z, \rho E)$	=	Fluid conservative variables	$p_{\text{ref}} = 2 \times 10^{-5}$ Pa	=	Reference pressure
$R(W, X)$	=	CFD numerical scheme	δ^*	=	Boundary layer displacement thickness
y^+	=	Dimensionless wall-distance			

*Associate Professor, Sorbonne Université, CNRS, Institut Jean Le Rond ∂'Alembert; antoine.hajczak@sorbonne-universite.fr
†Research Engineer, Aerodynamics Aeroelasticity Aeroacoustics Department; martin.buszyk@onera.fr.

I. Introduction

The most obvious aim of propeller blade design is to maximize the aerodynamic efficiency in view of reducing the energy consumption, and has accordingly been the subject of numerous work. In the early 90s, drawing on the maturity of physical models and computer programs, Dunn & Farassat [1] have focused on structural (aeroelasticity) as well as acoustic (aeroacoustics) constraints on top of aerodynamic performance. Addressing jointly these issues means in practice dealing with a multi-disciplinary optimisation problem and is currently the subject of active research, as shown by the European project MADELEINE (Multidisciplinary ADjoint-based Enablers for LargE-scale Industrial desigN in aEronautics, 2018-2021) [2] and the ongoing project NEXTAIR [3], in which this work is inscribed. Solving this problem can be formulated mathematically by introducing a set of n parameters $\alpha = (\alpha_1, \ldots, \alpha_n)^T$ that parameterize the blade shape. These shape parameters can include the blade radius, chord, twist, camber, or thickness distributions, *etc*. (see Fig. 1).

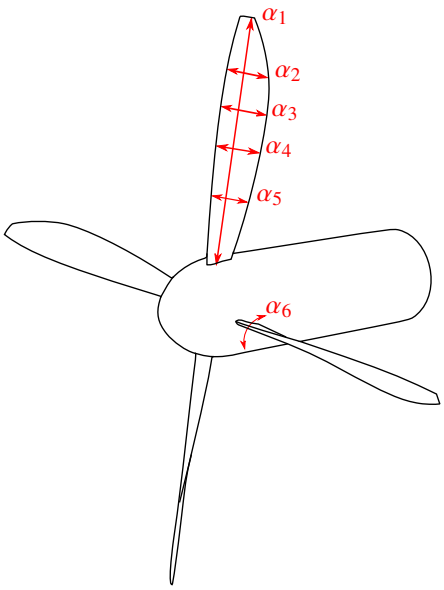

Fig. 1 Examples of typical propeller blade design variables.

As a first step toward a truly multidisciplinary optimization, the acoustic optimisation sub-problem is tackled in this paper. It involves a functional $\mathcal{J} : \alpha \rightarrow \mathcal{J}(\alpha)$ that provides a quantitative evaluation of the noise emitted by the propeller blades in rotating motion. This noise has both tonal and broadband noise components that result from various physical phenomena described for instance in [4]. A physics-based metrics such as the squared acoustics pressure at a given listener's position will be considered. Extension to more human-based metrics might incorporate psychoacoustics but are beyond the scope of this paper. In any case, the relation between $\mathcal{J}$ and the shape α is usually implicit. Therefore, it involves physical modelling, typically based on a hybrid CFD/CAA method in the traditional approach of the acoustic analogy. As for the optimization process, recent contributions include the use of evolutionary algorithms [5], as well as machine learning-based approaches [6]. Another approach that has received some attention lately is based on the determination of the objective function gradient $\mathrm{d}\mathcal{J}/\mathrm{d}\alpha$ using the adjoint method. In a computational fluid dynamics framework, this gradient can be expressed as a function of the partial derivatives $\partial\mathcal{J}/\partial X$ and $\partial\mathcal{J}/\partial W$, where X and W are the computational grid and the flow variables, respectively. Using this approach, Zhang & Barakos [7] have conducted the aerodynamic optimization of a ducted propeller. By means of an acoustic analogy, they have shown, but only *a posteriori*, that the aerodynamically optimal design leads to an improvement of the acoustics too. An application of the adjoint method to propeller noise was proposed by Chelius *et al.* [8] who used Hanson's model [9] to derive the squared acoustic pressure at a far-field listener. They have derived the analytical expression of the gradient of $\mathcal{J}$ by hand, which involved sensitivities of the propeller thrust and torque, that had previously been developed in Dumont's work on helicopter rotor optimization [10]. Hanson's model, however, only describes the propeller tonal noise at the blade passing frequency and its harmonics. In this work, we focus on the broadband component of a propeller noise spectrum. From a phenomenological perspective, propeller broadband noise is due (for an undisturbed upstream inflow) to the scattering of the turbulent structures inside the blade turbulent boundary layer by its trailing edge. Therefore, due

to the stochastic nature of turbulence, we suppose that the problem of minimizing the broadband trailing-edge noise of the entire propeller can be reduced to that of minimizing the broadband noise of independent blade radial portions. Moreover, the blade can be viewed as in a steady circular motion around the propeller axis, with no incidence and in a uniform mean flow. Thus, the full problem can be reduced to that of minimizing the trailing edge noise of 2D airfoil profiles mimicking individual propeller blade iso-radius cuts with a constant inflow velocity in the reference frame attached to the blade. Then, the noise generated by the entire blade could be obtained by summing the individual contributions of every strip, while including the Doppler effect associated with rotating motion [11, 12]. Thus, in this work, we focus on the shape optimisation of two-dimensional airfoil profiles.

The objective of this paper is to develop and validate an adjoint-based methodology to numerically estimate the sensitivities of a semi-analytical model for computing the broadband noise associated to the scattering of a turbulent boundary layer over a two-dimensional airfoil trailing-edge. To this end, we will use Amiet's model [13] in combination with semi-empirical wall pressure spectrum models at the airfoil trailing-edge. The sensitivities of these models with respect to the CFD grid X and the flow variables W are necessary to compute the derivative $\mathrm{d}\mathcal{J}/\mathrm{d}\alpha$ and will be obtained through the algorithmic differentiation (AD) tool Tapenade developed by INRIA [14]. The steady-state boundary layer integral quantities required by the semi-empirical models will be obtained using ONERA's Reynolds-Averaged Navier-Stokes (RANS) solver elsA and its adjoint [15]. After a presentation of both physical and numerical models in Sec. II, a verification of the forward aerodynamic and noise computations is then proposed in Sec. III.A for a low-speed symmetric NACA0012 airfoil with comparison to reference data, and in Sec. III.B for an asymmetric OAT15 profile more representative of future propeller applications at two Mach numbers. Then, the computation of the acoustic objective function sensitivities using the adjoint method is compared to traditional finite differences (FD) evaluations in Sec. III.C. A physical interpretation of the results, alongside with a discussion on the computational cost associated to both methods and perspectives are finally proposed in Sec. IV.

II. Methods

A. Physical modelling

1. Amiet's model and further extensions

The problem of thin airfoils trailing-edge noise is classically approached by approximating the airfoil as a semi-infinite plane. Doing so, Amiet [13] has proposed to combine Schwarzschild's solution [16] for the determination of the turbulent boundary layer wall pressure disturbance, and Curle's aeroacoustic analogy [17] for noise radiation. The extension of Amiet's solution to account for finite-chord effects has been proposed by Roger & Moreau [18]. For a far-field observer located in $\mathbf{x}$, the acoustic pressure autospectrum $S_{pp}(\mathbf{x},\omega)$ can be expressed as:

$$S_{pp}(\mathbf{x},\omega) = \left(\frac{\omega z L b}{2\pi c_0 S_0^2}\right)^2 \frac{1}{b}\int_{-\infty}^{+\infty} \Pi_0\left(\frac{\omega}{U_c}, K_y\right) \mathrm{sinc}^2\left[\frac{L}{2b}\left(\bar{K_y} - \bar{k}\frac{y}{S_0}\right)\right] \left|\mathcal{L}\left(\frac{\bar{\omega}}{U_c}, \bar{K}_y\right)\right|^2 \mathrm{d}\bar{K_y} \tag{1}$$

where L and b are the airfoil respective span and half-chord, quantities denoted $\overline{(\cdot)}$ being adimensioned by b. c_0 is the speed of sound, S_0 is the distance between the trailing-edge and the observer corrected for mean flow convection effects, U_c is the convection velocity of turbulence inside the boundary layer, K_y is the spanwise aerodynamic wavenumber and k is the acoustic wavenumber. $\mathcal{L}$ is the so-called airfoil transfer function, and is supposed to only be a function of the airfoil macroscopic dimensions L and b. Π_0 is the wavenumber spectral density of the incident turbulent gust. Equation 1 can be simplified, in the long span limit $L/b \gg 1$ as:

$$S_{pp}(\mathbf{x},\omega) = \left(\frac{\omega z b}{\pi c_0 S_0^2}\right)^2 \frac{L}{2}\left|\mathcal{L}\left(\frac{\bar{\omega}}{U_c}, \bar{k}\frac{y}{S_0}\right)\right|^2 \Phi_{pp}(\omega) l_y(k\frac{y}{S_0}, \omega). \tag{2}$$

In this latter expression, l_y represents the coherence length. We use Corcos' model following Roger & Moreau [18]. Finally, $\Phi_{pp}(\omega)$ is the autospectrum of wall-pressure disturbances near the trailing-edge region. It is the main input to the model for aeroacoustic predictions.

For a specified position $\mathbf{x}$, a straightforward overall acoustic objective function can be derived by taking the integral of the pressure far-field autospectrum over all frequencies. The result is normalised by an arbitrary multiplicative

constant Λ since we are mostly interested in variations of $\mathcal{J}$:

$$\mathcal{J}(S_{pp}) = \frac{\Lambda}{{p_{\text{ref}}}^2} \int_0^{+\infty} S_{pp}(\omega)\mathrm{d}\omega,\ p_{\text{ref}} = 20\ \mu\text{Pa} \tag{3}$$

Please note that there is no explicit relation between $S_{pp}(\omega)$ and α in Eq. 2. This is partly due to the fact that the airfoil is reduced to a finite flat plate of dimensions L and $2b$. Let us suppose furthermore that the airfoil chord is imposed. Then, the only dependence between the 2D airfoil shape (camber, thickness, etc) and the far-field pressure power spectral density is in the wall-pressure spectrum Φ_{pp}. Since the adjoint CFD solver in elsA is only stationary, a model is needed to relate boundary layer steady-state integral quantities near the trailing-edge, which are affected by a shape modification, to this spectrum.

2. Wall-pressure spectrum modelling from steady-state boundary layer variables

Wall-pressure spectrum modelling beneath a turbulent boundary layer has been extensively studied and a large panel of models exists that have been reviewed by Lee [19]. Among others, Goody's model accounts for Reynolds number variation effects, and Rozenberg's model has been widely used due to the fact that it allows taking into account adverse pressure gradients on cambered airfoils [20]. The analytical expression of such models can be quite involved and their derivatives with respect to the flow and geometry, accordingly, difficult to derive by hand. In the present work, we consider as a first step Amiet's model [13] that writes:

$$\frac{\Phi_{pp}(\omega)}{{\rho_0}^2 {\delta^*}{U_e}^3} = \frac{p_{\text{ref}}/2}{1 + \tilde{\omega} + 0.217\tilde{\omega}^2 + 0.00562\tilde{\omega}^4},\ \ \tilde{\omega} = \omega\delta^*/U_e \tag{4}$$

This model only involves the displacement thickness δ^* and the boundary layer outer velocity U_e that can be obtained from the computed vorticity field Ω as :

$$U_e(x) = \int_0^{+\infty} -\Omega(x,z)\mathrm{d}yz \tag{5}$$

$$\delta^*(x) = \frac{-1}{U_e(x)} \int_0^{+\infty} z\Omega(x,z)\mathrm{d}z \tag{6}$$

Using this model, Eq. 5 and 6 can be exactly differentiated with respect to the CFD grid and the flow variables. In this work, the integral over z is computed with the trapezoidal rule, and the vorticity $\vec{\Omega} = \vec{\nabla} \times \vec{v}$ is numerically computed using the Cartesian mesh Jacobian, the gradient operator being approximated with finite differences on the curvilinear mesh X used for airfoil computations. More advanced models require the boundary layer thickness which is not unequivocally defined for nonequilibrium flows and might involve non-C^1 functions [21] (regularity issues when using the discrete adjoint method are discussed by Peter [22]). Then, it appears that partial derivatives of Φ_{pp} with respect to X and W will involve partial derivatives of the boundary layer integral parameters U_e and δ^* which are not trivially implemented. To avoid deriving the sensitivities of the boundary layer integral parameters to X and W by hand, which is error-prone, and to allow further developments of the methodology with a physically more consistent wall pressure spectrum model, we use algorithmic differentiation to obtain the derivatives of the complex semi-analytical models.

B. Numerical modelling

1. Numerical evaluation of the objective function gradient

Formally, the optimisation problem to be solved is a minimization one:

$$\text{Find } \alpha^* \in D_\alpha \ \text{ such that } \mathcal{J}(\alpha^*) = \min \mathcal{J} \text{ where } D_\alpha \text{ is the vicinity of an } \textit{already acceptable shape } \alpha$$

It is important to note that the present approach is restricted to local optimisation only, so this methodology is not suited for finding disruptive blade designs, but rather improving an existing shape.

This problem can be approached very classically by determination of the gradient of $\mathcal{J}$ with respect to α, which is the n-sized vector of coordinates $\partial\mathcal{J}/\partial\alpha_i$ and using a descent algorithm. The relation between $\mathcal{J}$ and α is, as already stated in the introduction, not explicit. Specifically, for the present application, $\mathcal{J}$ is estimated using the physical modelling described in Eqs. 2 - 6 evaluated numerically using the flow conservative variable vector W and a computational grid X, on which the RANS equations, formally written $R(X, W) = 0$ in what follows, are solved.

A naive method to obtain the gradient of $\mathcal{J}$ is to use finite differences. For instance, using a central difference approximation, one would compute, $\forall i \leq n$ and with a small perturbation h of the i-th component α_i:

$$\frac{\mathrm{d}\mathcal{J}}{\mathrm{d}\alpha_i} = \frac{\mathcal{J}(\alpha + h) - \mathcal{J}(\alpha - h)}{2h}, \quad h \to 0 \tag{7}$$

The procedure is represented schematically in Fig. 2 where the red cells refer to RANS computations, while the blue cells refer to evaluations of Eqs. 2-6.

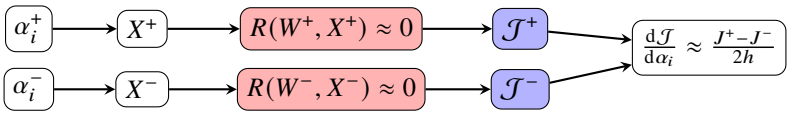

Fig. 2 Finite difference workflow to compute $\frac{\mathrm{d}J}{\mathrm{d}\alpha_i}$.

It is clear that using eq. 7 requires $2n$ RANS simulations, which is prohibitive for design when n is large. In that case, the adjoint method allows to obtain the gradient of $\mathcal{J}$ with a computation cost independent of n. Specifically, we use the discrete adjoint method, which can be introduced in several ways. A straightforward one, proposed by Peter [22], is briefly reproduced here. For a given shape, the RANS equations are solved:

$$R(W(\alpha), X(\alpha)) = 0 \tag{8}$$

Then, supposing that R is a C^1 function of X and W, by differentiation:

$$\frac{\partial R}{\partial W}\frac{\mathrm{d}W}{\mathrm{d}\alpha_i} + \frac{\partial R}{\partial X}\frac{\mathrm{d}X}{\mathrm{d}\alpha_i} = 0 \tag{9}$$

which can be multiplied by an arbitrary vector λ^T

$$\lambda^T\frac{\partial R}{\partial W}\frac{\mathrm{d}W}{\mathrm{d}\alpha_i} + \lambda^T\frac{\partial R}{\partial X}\frac{\mathrm{d}X}{\mathrm{d}\alpha_i} = 0 \tag{10}$$

Likewise, by differentiation of $\mathcal{J}$:

$$\frac{\mathrm{d}\mathcal{J}}{\mathrm{d}\alpha_i} = \frac{\partial \mathcal{J}}{\partial W}\frac{\mathrm{d}W}{\mathrm{d}\alpha_i} + \frac{\partial \mathcal{J}}{\partial X}\frac{\mathrm{d}X}{\mathrm{d}\alpha_i} \tag{11}$$

to which we can add Eq. 10 and obtain:

$$\frac{\mathrm{d}\mathcal{J}}{\mathrm{d}\alpha_i} = \left(\frac{\partial \mathcal{J}}{\partial W} + \lambda^T\frac{\partial R}{\partial W}\right)\frac{\mathrm{d}W}{\mathrm{d}\alpha_i} + \left(\frac{\partial \mathcal{J}}{\partial X} + \lambda^T\frac{\partial R}{\partial X}\right)\frac{\mathrm{d}X}{\mathrm{d}\alpha_i} \tag{12}$$

Equation 12 involves the term $\mathrm{d}W/\mathrm{d}\alpha_i$ of which computation is avoided if λ^T satisfies the *discrete adjoint equation*:

$$\frac{\partial \mathcal{J}}{\partial W} + \lambda^T\frac{\partial R}{\partial W} = 0 \tag{13}$$

Then, the gradient is expressed as:

$$\frac{\mathrm{d}\mathcal{J}}{\mathrm{d}\alpha_i} = \frac{\partial \mathcal{J}}{\partial X}\frac{\mathrm{d}X}{\mathrm{d}\alpha_i} + \lambda^T\frac{\partial R}{\partial X}\frac{\mathrm{d}X}{\mathrm{d}\alpha_i} \tag{14}$$

provided that we have computed λ^T beforehand from Eq. 13.

Since Eq. 13 does not involve α, it has to be solved only once and the result can be used for all shape parameters. The gain in computational cost compared to finite differences is then substantial when n is large. A schematic representation of the adjoint workflow is presented in Fig. 3 using the same color code as Fig. 2. It must be stressed once again that the output of the adjoint workflow is the sensitivities to all shape parameters whereas finite differences need to be repeated for all shape parameters. In this work, red cells are correspond to computations using elsA and its adjoint. The blue cells correspond once again to the physical models described in equations 2-6 but this time their partial derivatives with respect to X and W are needed. These derivatives can either be differentiated by hand, which is tedious and error-prone, or differentiated using algorithmic differentiation. The latter strategy has been retained here. Finally, a numerical tool is

needed to provide the sensitivities of X to the shape parameters. This part of the workflow has been highlighted in green. Details about the three aforementioned parts are given in the following subsections.

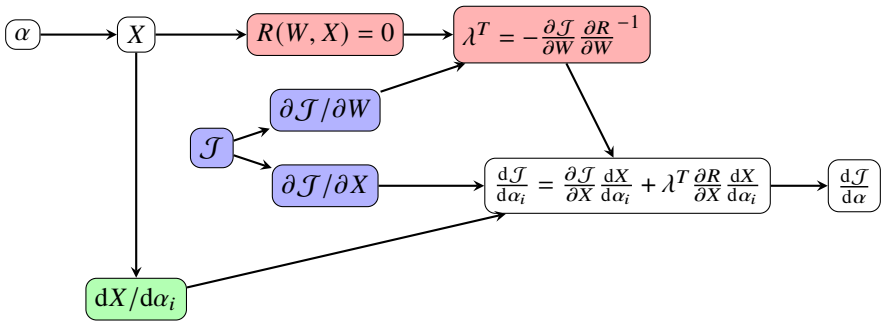

Fig. 3 Schematic representation of the workflow used to obtain the gradients of the acoustic objective function. In red: CFD part, in blue: acoustic objective function, and in green: computational grid deformation.

2. Reynolds-Averaged Navier-Stokes forward and adjoint solvers

The forward RANS simulations around the airfoil profiles are carried out using ONERA's solver elsA [23] on Cartesian multiblock curvilinear grids fitted to the airfoil surface using a finite-volume, cell-centered formulation. Convective fluxes are discretized with a Roe upwind scheme and a van Albada slope limiter. The pseudo-time stepping scheme used is Backward Euler with an LU-SSOR implicit stage. The Spalart-Allmaras model is used for turbulence. The computation of the adjoint vector λ is solved using a preconditioned General Minimum RESidual (GMRES) algorithm [24] featuring 10 inner sub-iterations in a Krylov space of dimension 60. The linearised Spalart-Allmaras (SAlin) turbulence model is preferred to the so-called frozen-μ_t approach, usually considered more robust but also less precise, for adjoint computations. More details about the implementation of the SAlin model within elsA can be found in [25].

3. Algorithmic differentiation

According to the previous sections, $\mathcal{J}$ is a composed function of several models for a given X and W. In fact, only a small portion of the computational domain is used by the models, since the useful information is the boundary layer displacement thickness and convective velocity at a selected point close to the trailing-edge. In the present discrete adjoint framework, all these functions have been implemented as Fortran 90 programs. Following the chain rule, the derivatives of $\mathcal{J}$ with respect to X and W, needed for the gradient computation (see Fig. 3), require the derivatives of intermediate functions. Instead of deriving by hand and implementing the expressions, the associated derivatives are obtained as Fortran sources as well, using the Algorithmic Differentiation (AD) tool Tapenade [14] developed by INRIA. This tool builds additional Fortran sources containing the derivatives of the forward program's selected output(s) with respect to selected input(s).

4. Sequential Analytical Deformation

The final gradient with respect to α requires the previously discussed derivative with respect to the grid nodes X be multiplied by $\mathrm{d}X/\mathrm{d}\alpha$. This latter term is evaluated using an in-house Sequential Analytical Deformation (SeAnDef) tool, which additionally provides the deformed grids $X(\alpha^+)$ and $X(\alpha^-)$ to allow finite differences comparisons with adjoint computations. The purpose of SeAnDef is to compute parametric grid deformations of complex geometries which have a main axis along which the user can parameterize the surface at given control points and sections. Surface deformations are then propagated to the entire volumic grid. Various deformation parameters are included, such as twist, translation, thickness, camber, or local deformation. For clarity, the focus in what follows will be on local thickness and camber only. Other successful shape optimizations using SeAnDef can be found for instance in Meheut *et al.* [26].

III. Results

A. Validation of the forward computation on a NACA0012 airfoil

The forward aerodynamic and acoustic numerical solutions are first validated on a classical trailing-edge noise case: a NACA0012 airfoil of chord $c = 2b = 6.096 \times 10^{-1}$ m and span $L = 4.6 \times 10^{-1}$ m in a low Mach number flow of 0.2048 with no incidence. The boundary layer at the trailing-edge can be considered turbulent as the chord-based Reynolds number is $\mathrm{Re}_c = 2.85 \times 10^6$. Reference data for this case are to be found in the experiments of Brooks & Hodgson [27] which include acoustic measurements. Turbulent boundary layer quantities are compared to reference values obtained by Rozenberg *et al.* [20] using the code XFOIL.

The forward RANS computation (red cells in Fig. 3) is carried out on a Cartesian mesh with 300 points on the airfoil contour. The stretching of the cells normal to the wall is such that $y^+ = 0.5$ on the initial layer in order to correctly capture the boundary layer development. A cell size growth rate of 10% (Fig. 4a) is then imposed to keep an acceptable cell count.

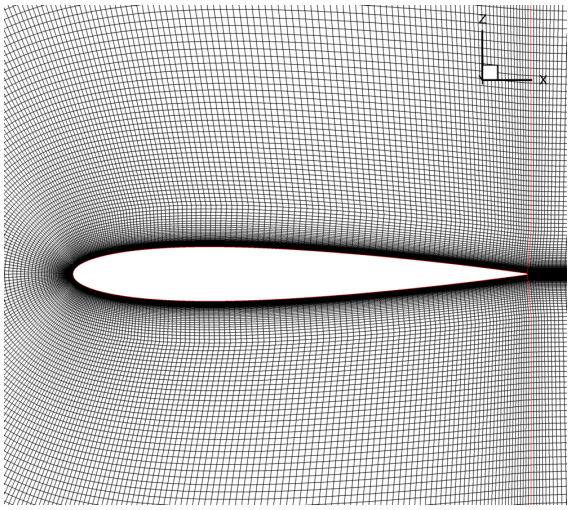

(a) Computational grid used for the forward RANS computation around the NACA0012 profile.

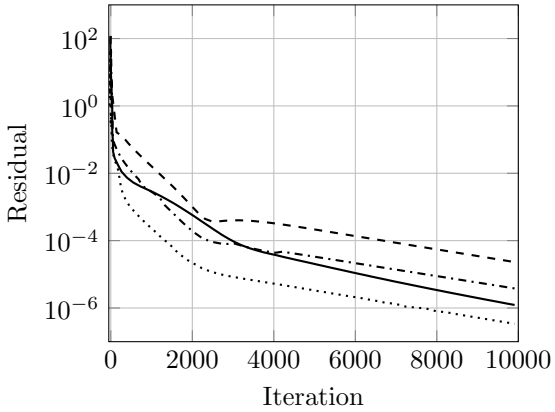

(b) Residual of the forward RANS simulations on the NACA0012 profile. Solid: ρ, dashed: ρv_x, dotted, ρv_z, dash-dotted: ρE

Fig. 4 Computational grid and residuals for the forward NACA0012 RANS computation.

The adjoint method heavily relies on the implicit functions theorem which requires the CFD computation to be perfectly converged. This means that Eq. 8 must be satisfied with the best possible precision. Figure 4b presents the residual of the Navier-Stokes system as a function of the number of iterations. This residual drops by at least six orders of magnitude after 10^4 iterations. The simulation is then supposed well converged.

1. Verification of boundary layer parameters

The boundary layer parameters used in Amiet's wall pressure spectrum model (Eq. 4) are compared to XFOIL 6.9 simulations provided by Rozenberg *et al.* [20] in Tab. 1 and 2. Although the airfoil considered is symmetrical, computed boundary layer quantities are presented for both the pressure and suction sides. The values obtained are identical to 1 or 2-digits precision, supporting the good convergence of the flow already suggested by Fig. 4b. The values of δ^* and U_e are computed using Eqs. 5 and 6 with the assumption that the mesh is locally orthogonal to the profile in the region where Ω varies substantially, allowing the numerical integration to be calculated directly using the values of the flow at the mesh nodes. This approximation proved to be reasonable with the chosen grid. The error at $x/c = 0.87$ is 14% for displacement thickness, but the agreement is more satisfying closer to the trailing-edge, at $x/c = 0.97$ where the error drops to 6% with respect to XFOIL data. In terms of external velocity, the agreement is remarkable with relative errors of 0.2% at $x/c = 0.87$ and 1% at $x/c = 0.97$.

	δ^* ($\times 10^{-3}$ m)	U_e (m/s)
Rozenberg *et al.*	1.62	69.3
Present - SS/PS	1.85/1.84	69.42/69.52
Relative error	14%	0.2%

Table 1 $x/c = 0.87$

	δ^* ($\times 10^{-3}$ m)	U_e (m/s)
Rozenberg *et al.*	2.36	64.6
Present SS/PS	2.50/2.52	65.22/65.13
Relative error	6%	1%

Table 2 $x/c = 0.97$

Comparison of boundary layer characteristics obtained with the forward RANS solver and XFOIL data.

2. Verification of noise spectrum

Combining Amiet's theory (Eq. 2) with the wall-pressure spectrum model (Eq. 4) evaluated with δ^* and U_e averaged between pressure and suction sides at $x/c = 0.97$, we can compare the noise spectrum for a listener located at $z = 1.2$ m above the trailing-edge, at the same location as Brooks & Hodgson's experiment [27]. The agreement between the prediction and the experimental data shown in Fig. 5, reaches a 1 dB precision between 2 and 3 kHz. At lower and higher frequencies, the general shape of the noise spectrum is approximately captured but errors of several dB are observed. These errors are most likely due to two inappropriate approximations. The first one is that $L/b \simeq 1.5$, which makes the approximation used to derive expression 2 debatable. The second point is that the wall-pressure spectrum model used is rather basic and incorporates neither Reynolds nor adverse pressure gradient effects. Rozenberg's model has shown more precise on this particular case (see Fig. 21 in [20]) but, as already mentioned in II.A.2, concerns about boundary layer thickness not being regular enough prevented the use of more advanced models. Overcoming this difficulty will be the key to improving the method. Despite this lack of precision, gradient estimations might however be valid since it is the variations in the noise spectra that are of interest here, rather than the absolute values of the noise spectra.

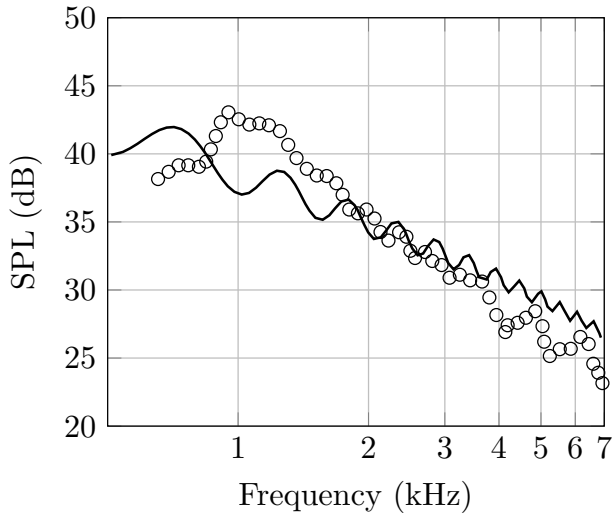

Fig. 5 Far-field broadband trailing-edge noise (–) predicted compared against (∘) experimental data from Brooks & Hodgson [27].

B. Forward computation on a more relevant test-case for future propeller applications: OAT15 profile in subsonic and transonic conditions

The NACA0012 results can readily serve as a basis for airfoil trailing-edge noise. They also prove that the forward part of the methodology gives physically sound results. A second test-case has been selected for subsequent gradient evaluations since the final aim of this work is propeller blade optimization, which present non-symmetric profiles as well as possible high Mach numbers, especially close to the blade tip. Accordingly, a supercritical ONERA OAT15 profile [28], which is also currently the subject of other adjoint-based aerodynamic optimization studies, (see *eg* Jadoui *et al.*

[24]), is considered in the following. This time, only suction side integral quantities are used for noise computations, following Finez [29]. The near-wall grid spacing is similar to the NACA0012 case. The method is assessed for two inflow Mach numbers ($M = 0.2, Re_c = 5.5 \times 10^6$) and ($M = 0.734, Re_c = 20.3 \times 10^6$), corresponding to subsonic and transonic conditions, respectively, representative for instance of blade positions closer to either the hub or the tip. The validity of the Amiet's trailing-edge noise model in the presence of a shock has been questioned recently by Koch *et al.* [30]. They have shown correct far-field predictions at 90° from the mean flow direction around a transonic airfoil. Therefore, Eq. 2 will be used both in subsonic and transonic conditions.

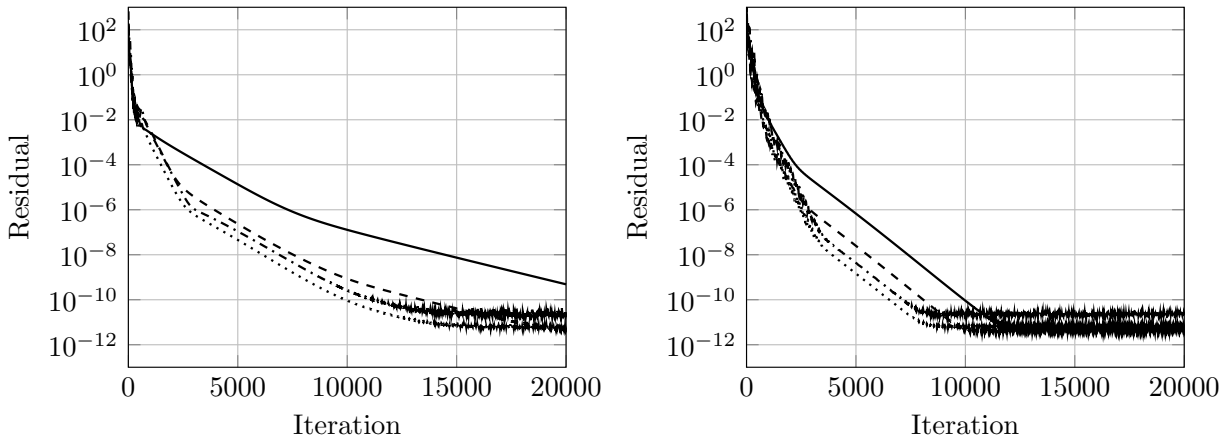

(a) M=0.2 (b) M=0.734

Fig. 6 Residual of the forward RANS simulations on the OAT15 profile. Solid: ρ, dashed: ρv_x, dotted, ρv_z, dash-dotted: ρE

Once again, the convergence of RANS simulations for both values of the inflow Mach number is provided in Fig. 6 where the decrease by several orders of magnitude in the residual values suggests the convergence of the numerical simulation. The subsonic case shows however a noticeably slower convergence, about twice as many iterations than the transonic one for an equivalent target residual value for all variables but the density which presents an especially slow decay.

Mach contour maps of the steady-state solution are illustrated in Fig. 7. On the transonic profile, the normal shock wave has a very distinct influence on the boundary layer development. As will be discussed later on, a high sensitivity of the noise results is then to be expected in transonic conditions, especially with respect to the shockwave position. This, again, clearly indicates the relevance of aerodynamic and acoustic multi-disciplinary optimization. The green line over-plotted at $x/c = 0.9$ in Fig. 7 presents the region of interest for boundary layer integral quantities evaluation.

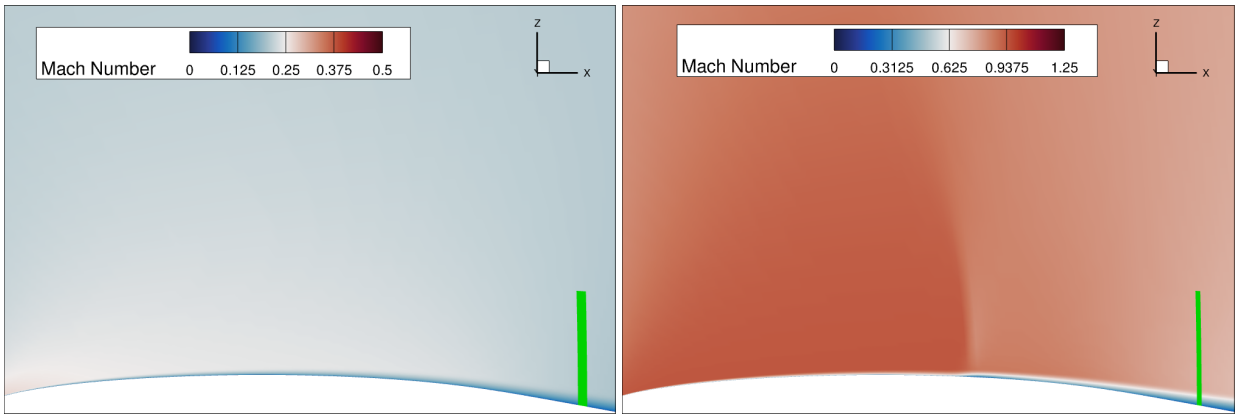

(a) M=0.2 (b) M=0.734

Fig. 7 Mach number contour maps (zoom on the OAT15 geometry).

C. Validation of the adjoint chain by comparison with finite differences

1. Verification of the objective function derivatives w.r.t. X and W and implementation of the adjoint computation

Intermediate sensitivities of $\mathcal{J}$ with respect to X and W are usually compared to finite differences evaluations. Specifically, this validates the blue cells in Fig. 3. To do so, small variations are imposed to the volume grid X and the flow field W obtained with the forward computation previously described. The sensitivities are then computed in two ways. First, finite differences are performed. Let V designate either X or W and V_{ij} a particular value at either the cell center (for W) or node location (for X) of indices (i, j). For each point of the Cartesian grid, the partial derivative is obtained using a central difference approximation, with $\Delta V_{ij} = 10^{-7}$, as:

$$\frac{\partial \mathcal{J}}{\partial V_{ij}} = \frac{\mathcal{J}(V + \Delta V_{ij}) - \mathcal{J}(V - \Delta V_{ij})}{2\Delta V_{ij}}$$

Secondly, these derivatives are obtained directly using differentiated Fortran sources built with Tapenade (see II.B.3).

The comparison between AD and FD is presented for space (x and z) and flow (ρ, ρv_x, ρv_z) variables in figures 8 (subsonic flow) and 9 (transonic flow), as a function of the position z at $x/c = 0.9$ (green line in Fig. 7). Several general remarks can be made about these figures. First, it is evident that the sensitivities obtained through AD are correctly implemented since they perfectly match the ones obtained with FD. Furthermore, for all variables, the sensitivities increase, in absolute value, with increasing z. One must however bear in mind that shape modifications will mostly affect z positions close to zero so the apparent diverging behavior is in practice compensated by the local character of shape-induced grid and flow variations. It is also noteworthy that the general shape of the curves is conserved between the subsonic and transonic cases despite the second case involving substantially different physical content. Looking at the absolute values however, it appears that the transonic case is two to three orders of magnitude more sensitive than the subsonic one to variations in X or W, as already inferred from Mach number contours examination in Fig. 7.

Now, looking at the resolution of the adjoint equation 13 with the GMRES algorithm detailed in II.B.2 for a target residual of 10^{-10}, similar conclusions about the convergence rate shown in Fig. 10 can be made as for the forward computation. Indeed, it takes about twice as many iterations to reach the target residual for the subsonic case than for the transonic one.

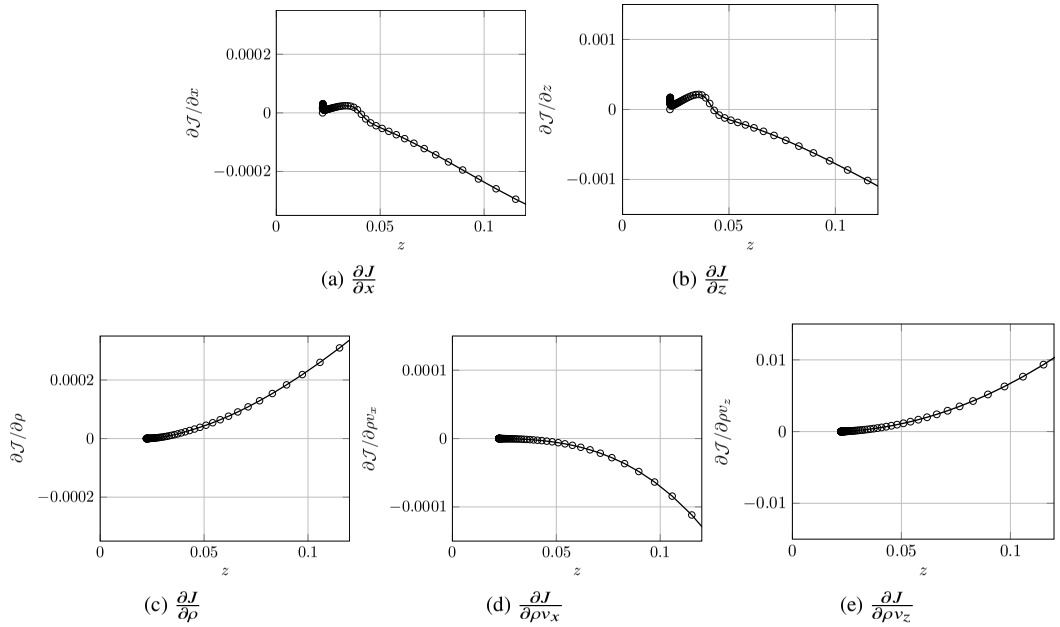

Fig. 8 Comparison between X and W sensitivities obtained using FD (–) and AD (○) on the $M = 0.2$ OAT15 profile.

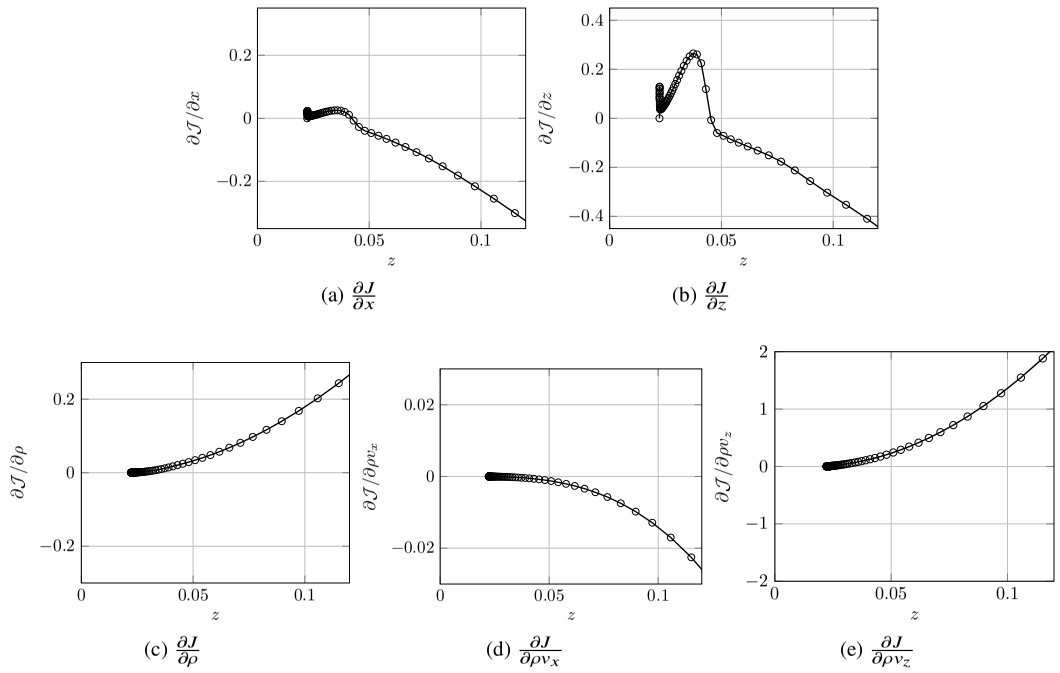

Fig. 9 Comparison between X and W sensitivities obtained using FD (–) and AD (○) on the $M = 0.734$ OAT15 profile.

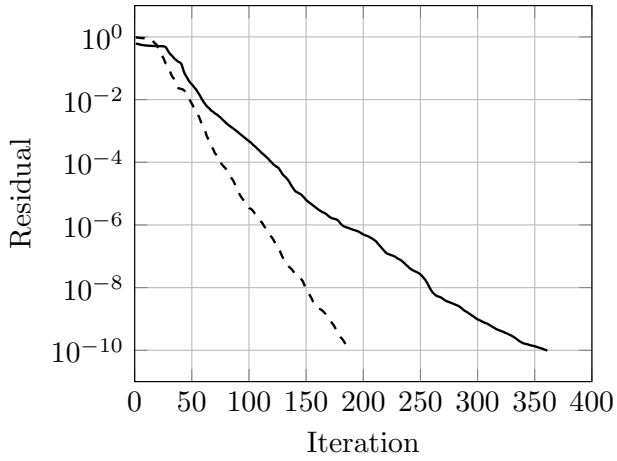

Fig. 10 GMRES residual of the adjoint calculation. Solid line: $M = 0.2$**. Dashed line:** $M = 0.734$

2. Verification of the objective function gradients w.r.t. α

The gradient $\mathrm{d}\mathcal{J}/\mathrm{d}\alpha$ is finally obtained by multiplying the so-called "adjoint-mesh" solution $\mathrm{d}J/\mathrm{d}X(\alpha)$ by the grid sensitivity $\mathrm{d}X/\mathrm{d}\alpha$ which is given by SeAnDef. To assess the validity of this gradient, we consider two shape parameters, namely camber and thickness at three specified positions x/c of 0.25, 0.5 and 0.75. A simple approach is again to consider finite differences with a centered scheme:

$$\frac{\partial \mathcal{J}}{\partial \alpha_i} = \frac{\mathcal{J}(\alpha_i + \Delta\alpha_i) - \mathcal{J}(\alpha_i - \Delta\alpha_i)}{2\Delta\alpha_i} \tag{15}$$

For each partial derivative with respect to a shape parameter α_i, two RANS computations are then needed, resulting here in two shape parameters $\times$ three locations $\times$ two evaluations for the centered scheme, for a total of 12 RANS simulations. Exaggerated deformations applied on the OAT15 geometry provided by SeAnDef corresponding to each RANS simulation are shown in Figs. 11,12,13, and 14. Moreover, as the finite difference approach only provides an approximation of the derivative values, several step sizes $\Delta\alpha_i$ have been considered for each deformation, thus multiplying the number of required computations to assess the convergence of FD as well.

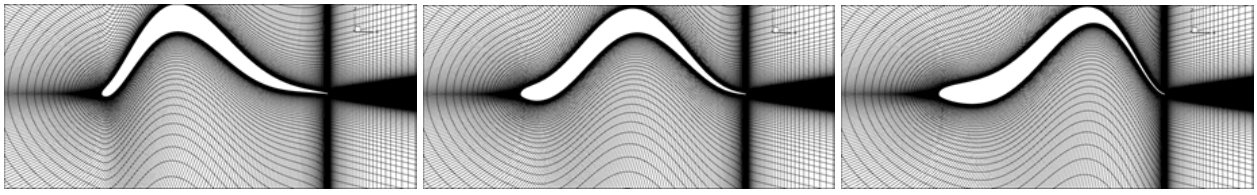

(a) 25% of the chord (b) 50% of the chord (c) 75% of the chord

Fig. 11 Exaggerated camber deformations (positive direction).

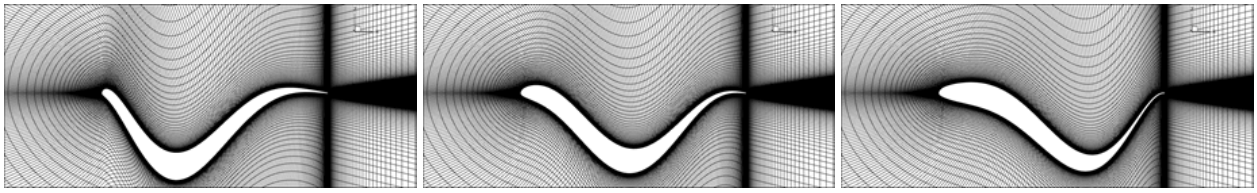

(a) 25% of the chord (b) 50% of the chord (c) 75% of the chord

Fig. 12 Exaggerated camber deformations (negative direction).

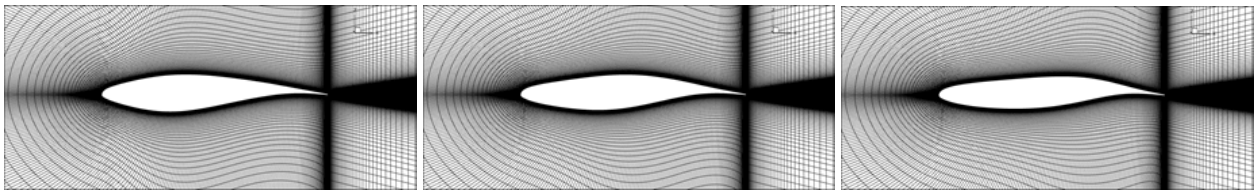

(a) 25% of the chord (b) 50% of the chord (c) 75% of the chord

Fig. 13 Exaggerated thickness deformations (positive direction).

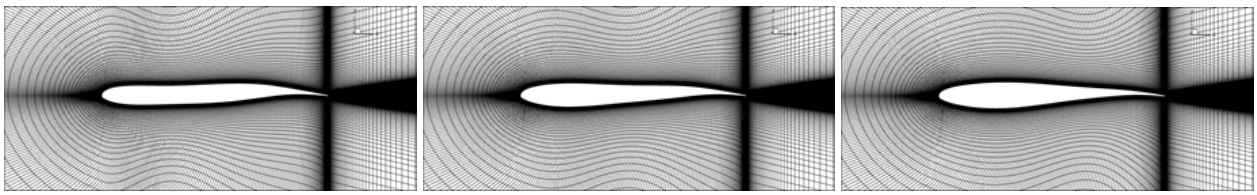

(a) 25% of the chord (b) 50% of the chord (c) 75% of the chord

Fig. 14 Exaggerated thickness deformations (negative direction).

The sensitivity to each parameter, obtained following both adjoint and FD methods, is finally compared in Figs. 15 and 16. The examination of these results confirms once again that the sensitivities are, in absolute value, much larger for the transonic profile than for the subsonic one. Accordingly, FD evaluations converge faster for the subsonic case than for the transonic case, at equivalent finite difference step and for a given shape parameter. In other words, the higher the sensitivity to a shape parameter is, the finer the FD step is needed to get a correct approximation of the gradient. Now comparing converged FD (filled circles) with the adjoint method (filled triangles), we can see that the agreement between both approaches is very good on camber at subsonic and transonic speeds, with a slight loss of agreement as the deformation is imposed closer to the trailing-edge. Looking at the thickness, the evolution of the sensitivity with the position on the profile follows the same trend between adjoint and FD evaluations, but, for each Mach number, a nearly constant value separates adjoint and FD values. This difference is $\sim 2 \times 10^{-5}$ at $M = 0.2$ and $\sim 2.5 \times 10^{-2}$ at $M = 0.734$. The origin of this constant error is still under investigation.

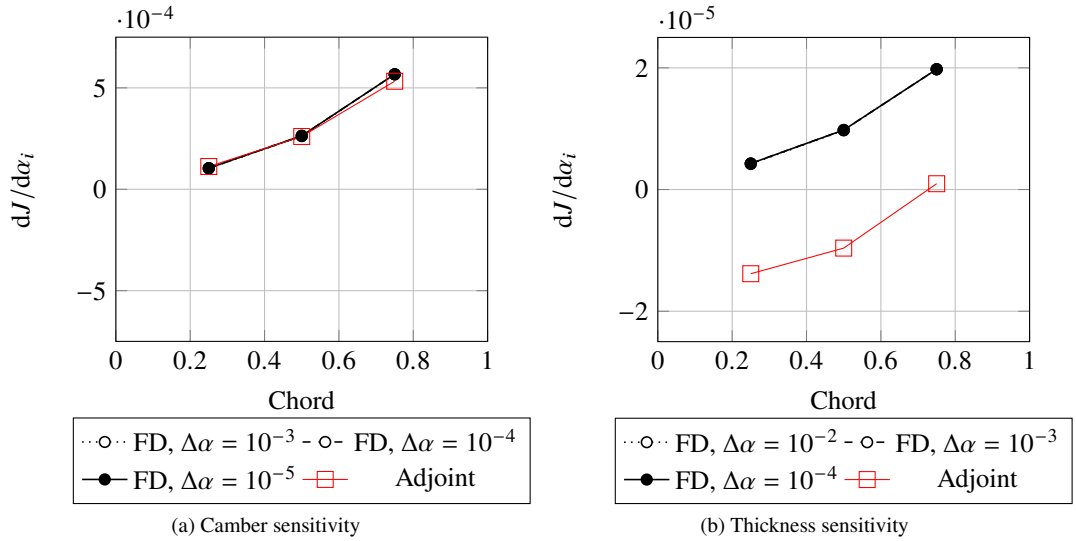

(a) Camber sensitivity (b) Thickness sensitivity

Fig. 15 Trailing-edge noise sensitivities of the OAT15 profile at $M = 0.2$.

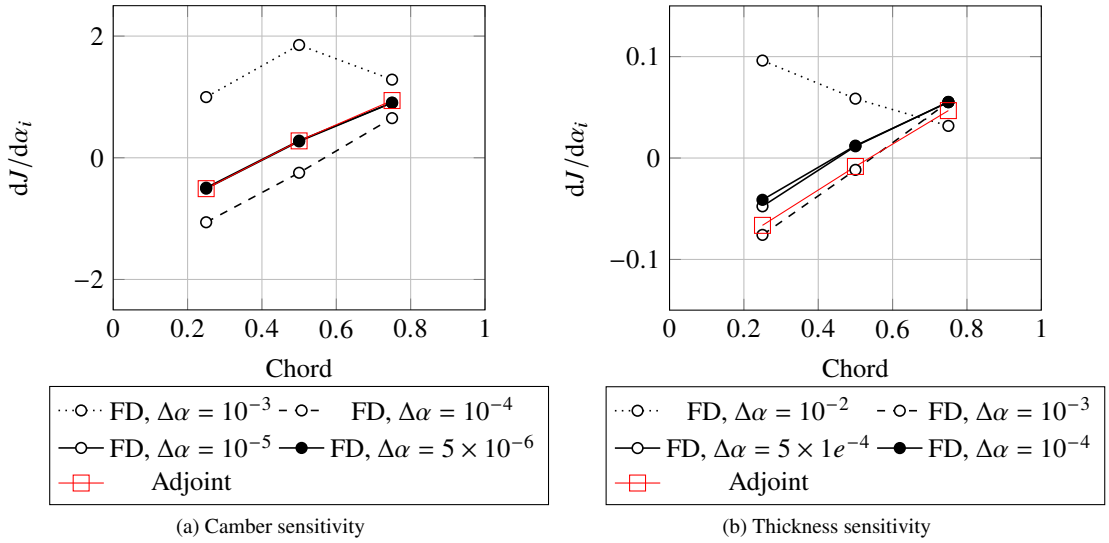

(a) Camber sensitivity (b) Thickness sensitivity

Fig. 16 Trailing-edge noise sensitivities of the OAT15 profile at $M = 0.734$.

D. Variation in sound spectrum for deformed shape w.r.t. the baseline case

According to Figs. 15 and 16, the largest variation in trailing-edge noise for all considered cases is to be expected for an increase in camber at $x/c = 0.75$ at $M = 0.734$. As shown in Fig. 17a, the shock position is quite sensitive to a small camber increase of $\Delta\alpha = 10^{-3}$ (please note that the shape variation is too small to be observable on the figure). In this case, the shock is moved downstream of its initial location when camber is increased. This affects the subsequent boundary layer development. Recalling that $\mathcal{J}$ is integrated over all frequencies and scaled by a constant, the absolute value of the gradient is not easily interpreted. The effective variation in SPL is plotted in Fig. 17b to determine the orders of magnitude that can be expected for this shape modification.

For this modification in camber close to the trailing-edge, the increase in SPL is not uniform across all frequencies. It is about 0.1 dB at low frequencies and decreases to about 0.04 dB at 7 kHz. This variation must be understood as only one step in the optimization loop, so larger variations are expected when several steps have been performed. Future

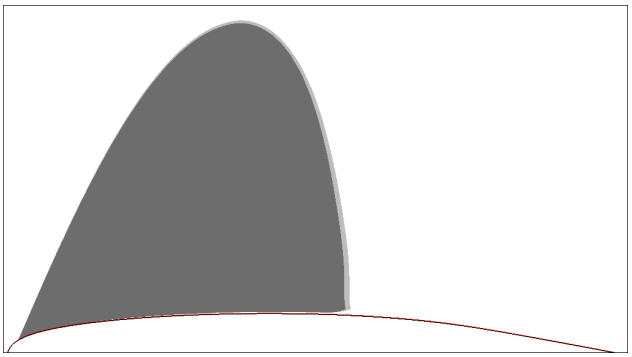

(a) Isocontour $M = 1$ of the (–) baseline and (–) deformed OAT15 profiles. Light gray: camber increase of 10^{-3}. Dark gray: camber decrease of 10^{-3}.

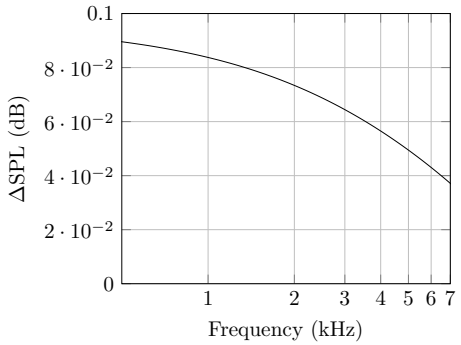

(b) Variation in SPL for a small increase in camber at $x/c = 0.75$ w.r.t. the baseline $M = 0.734$ OAT15 profile.

Fig. 17 Variations of the Mach number field and SPL for a small camber variation on the OAT15 profile at $M = 0.734$.

work will be devoted to running the entire optimization loop to determine if the optimization converges to a minimum, and if so, in how many steps, for which global SPL variation. Coupling with aerodynamic constraints will likely be crucial to convergence of the optimization process while retaining a realistic shape.

IV. Discussion

From a physical point of view, the results might be interpreted as follows. First, the transonic profile is much more sensitive to shape deformations than the subsonic one for trailing-edge noise. Second, applying a camber increase on the subsonic profile results in a noise increase for all three positions considered since the gradient is strictly positive. This is not the case for the transonic profile where a camber increase at $x/c = 0.25$ implies a decrease in the noise predicted. This would be consistent with the intuition that the shock location (and, thus, the boundary layer state downstream) might also be highly sensitive to upstream camber. Determining if a decrease in noise would also come with an improvement of the aerodynamic performance will be the subject of future investigations, as proper multi-disciplinary optimization will be carried out. In both cases, the sensitivity absolute value is larger as the deformation takes place closer to the trailing-edge, which could have been anticipated, since this is the region where the acoustic source is active. The same conclusions might be drawn from thickness sensitivities if the FD gradients are considered. Here again, adjoint-based gradients must be further investigated by (i) working on the mesh deformation propagation, currently artificially limited to the z line over which boundary layer integral quantities are computed and (ii) integrating over a line actually normal to the profile rather than following the grid. This would require an additional interpolation step. In the current state of this work, the sign of thickness adjoint sensitivities is not reliable and cannot be used in the optimization chain yet. For a small camber variation, the resulting difference in SPL is a fraction of dB, which may add up during the optimization process.

The main motivation for using the adjoint method is the gain in computational cost associated to the gradient estimation. In this respect, it is worth noting that the adjoint simulation took around 5 minutes on 16 cores, regardless of the parameter space dimension, the final assembly of the gradient being carried out afterwards. On the other hand computing the gradient of $\mathcal{J}$ with centered FD took about 80 minutes on 16 cores $\times$ 2 evaluations for each design variables. It should be emphasized that here a total of six shapes parameters have been considered, so the gain is, as expected, substantial, thus supporting the relevance of adjoint-based methods in combination with semi-empirical modelling. This computation time could also be further reduced if the target residual in the GMRES algorithm is decreased. Fine tuning of this parameter will be investigated in future work as a perspective to improve the method efficiency.

Despite these advantages, the work presented here is based on some strong assumptions which will require some careful inspection. A first concern is about the contrast in the simpleness of the physical modelling and the effective variations in the objective function. Indeed, real variations might be overwhelmed by approximation errors. For example, the flat-plate assumption in Amiet's model hides possible X dependencies and may seem contradictory with the objective of performing shape optimization, although this model is routinely used for airfoil trailing-edge noise

evaluations. This paradox is however only partial since a dependency on W is still present through wall pressure modelling. High-fidelity simulations of the final supposed optimal shape will be necessary to confirm the result of the optimization process as well as aerodynamic performance constraints. Similarly, imposing camber variations clearly calls for the use of wall-pressure spectrum models that take into account adverse pressure gradients, such as the one proposed by Rozenberg *et al.* [20]. This extension will be considered in future work too. Another important assumption is that local optimization of blade sections will result in a smooth and optimal blade shape. The extent of independent blade sections to be considered might be dependant on the coherence length over the trailing edge. Such aspects will be considered as single airfoil optimization will be available. A long-term solution to the points raised above is to replace the semi-empirical modelling (Hanson's model in Chelius *et al.* [8], or Amiet's model in this work) by an adjoint formulation of the acoustic analogy. This work has been initiated at ONERA with the development of an adjoint formulation of the FW-H integral equation.

V. Conclusion

An adjoint-based methodology has been proposed with the final aim of performing propeller blade shape optimization. This paper has been devoted to exposing the methodology, which relies on the combined use of Amiet's semi-empirical wall-pressure spectrum model and trailing-edge noise model over two-dimensional airfoils. The inputs to these models are determined using steady CFD solutions obtained with ONERA's RANS solver elsA, as well as its adjoint. The inputs to the adjoint solver, which are the objective function's sensitivity to the computational grid and flow variables and the grid sensitivity to shape parameters are provided by the algorithmic differentiation tool Tapenade and the sequential analytical deformation tool SeAnDef, respectively. The forward aerodynamic and acoustic computations have first been validated over a classical trailing-edge noise database on a subsonic and symmetric NACA0012 airfoil. Then, an asymmetric OAT15 profile at both subsonic and transonic speeds has been considered in order to evaluate the methodology on profiles more similar to propeller blade sections. Partial derivatives of the objective function with respect to the grid and flow have been compared to finite differences evaluations, showing a perfect agreement and confirming the effectiveness of AD in providing differentiated Fortran sources for adjoint evaluations. Then, the gradient of the objective function has been evaluated with respect to two shape parameters, namely camber and shape, for both Mach numbers considered, and compared to FD evaluations. Again, adjoint-based and FD evaluations have shown a very good agreement at both Mach numbers for camber, but partially inconclusive results have been obtained for thickness sensitivities. Values obtained using adjoint-based computations systematically present a constant difference with FD. The origin of this discrepancy is currently under investigation. Finally, considering the most sensitive camber variation, the difference in SPL has been evaluated. In this case, it caused a variation in SPL by about 0.1 dB in the low frequency range. These results show the first use of an adjoint-based method with semi-empirical modelling to perform airfoil shape optimization of trailing-edge noise and offer perspectives for designing more quiet propeller blades.

Acknowledgments

The NEXTAIR project has received funding from the European Union's HORIZON Research and Innovation Actions program under grant agreement No 101056732.

References

[1] Dunn, M., and Farassat, F., "State-of-the-art of high-speed propeller noise prediction-A multidisciplinary approach and comparison with measured data," *13th Aeroacoustics Conference*, 1990, p. 3934.

[2] MADELEINE Consortium, "Design Procedure and Multu-Discplinary Optimisation in Aeronautics," , . URL `https://www.madeleine-project.eu/`.

[3] NEXTAIR Consortium, "Multi-disciplinary digital - enablers for NEXT-generation AIRcraft design and operations," , . URL `https://www.nextair-project.eu/`.

[4] Hubbard, H. H., "Aeroacoustics of flight vehicles: Theory and practice. volume 1. noise sources," *NASA reference publication*, Vol. 1258, 1991.

[5] Marinus, B., Roger, M., and Van Den Braembussche, R., "Aeroacoustic and aerodynamic optimization of aircraft propeller blades," *16th AIAA/CEAS aeroacoustics conference*, 2010, p. 3850.

[6] Geng, X., Liu, P., Hu, T., Qu, Q., Dai, J., Lyu, C., Ge, Y., and Akkermans, R. A., "Multi-fidelity optimization of a quiet propeller based on deep deterministic policy gradient and transfer learning," *Aerospace Science and Technology*, Vol. 137, 2023, p. 108288.

[7] Zhang, T., and Barakos, G. N., "High-fidelity numerical analysis and optimisation of ducted propeller aerodynamics and acoustics," *Aerospace Science and Technology*, Vol. 113, 2021, p. 106708.

[8] Chelius, A., El Din, I. S., and Koch, R., "Toward an Adjoint Based Aeroacoustic Optimisation for Propeller Noise Reduction," *ICSV26*, 2019.

[9] Hanson, D. B., "Helicoidal surface theory for harmonic noise of propellers in the far field," *AIAA journal*, Vol. 18, No. 10, 1980, pp. 1213–1220.

[10] Dumont, A., Le Pape, A., Peter, J., and Huberson, S., "Aerodynamic shape optimization of hovering rotors using a discrete adjoint of the Reynolds-Averaged Navier–Stokes Equations," *Journal of the American Helicopter Society*, Vol. 56, No. 3, 2011, pp. 1–11.

[11] Schlinker, R., and Amiet, R., "Helicopter rotor trailing edge noise," *7th Aeroacoustics Conference*, 1981, p. 2001.

[12] Sinayoko, S., Kingan, M., and Agarwal, A., "Trailing edge noise theory for rotating blades in uniform flow," *Proceedings of the Royal Society A: Mathematical, Physical and Engineering Sciences*, Vol. 469, No. 2157, 2013, p. 20130065.

[13] Amiet, R. K., "Noise due to turbulent flow past a trailing edge," *Journal of sound and vibration*, Vol. 47, No. 3, 1976, pp. 387–393.

[14] Hascoët, L., and Pascual, V., "Tapenade 2.1 user's guide," Tech. rep., INRIA, 2004.

[15] Peter, J., "Discrete adjoint method in elsA (part I): method/theory," *Proceedings of the ONERA-DLR Aerospace Symposium (ODAS), Toulouse*, 2006.

[16] Schwarzschild, K., "Die beugung und polarisation des lichts durch einen spalt. i," *Mathematische Annalen*, Vol. 55, No. 2, 1901, pp. 177–247.

[17] Curle, N., "The influence of solid boundaries upon aerodynamic sound," *Proceedings of the Royal Society of London. Series A. Mathematical and Physical Sciences*, Vol. 231, No. 1187, 1955, pp. 505–514.

[18] Roger, M., and Moreau, S., "Back-scattering correction and further extensions of Amiet's trailing-edge noise model. Part 1: theory," *Journal of Sound and vibration*, Vol. 286, No. 3, 2005, pp. 477–506.

[19] Lee, S., "Empirical wall-pressure spectral modeling for zero and adverse pressure gradient flows," *AIAA Journal*, Vol. 56, No. 5, 2018, pp. 1818–1829.

[20] Rozenberg, Y., Robert, G., and Moreau, S., "Wall-pressure spectral model including the adverse pressure gradient effects," *AIAA journal*, Vol. 50, No. 10, 2012, pp. 2168–2179.

[21] Griffin, K. P., Fu, L., and Moin, P., "General method for determining the boundary layer thickness in nonequilibrium flows," *Physical Review Fluids*, Vol. 6, No. 2, 2021, p. 024608.

[22] Peter, J., "Contributions to discrete adjoint method in aerodynamics for shape optimization and goal-oriented mesh-adaptation," , 2020. Habilitation manuscript, Université de Nantes.

[23] Cambier, L., Heib, S., and Plot, S., "The Onera elsA CFD software: input from research and feedback from industry," *Mechanics & Industry*, Vol. 14, No. 3, 2013, pp. 159–174.

[24] Jadoui, M., Blondeau, C., Martin, E., Renac, F., and Roux, F.-X., "Comparative study of inner–outer Krylov solvers for linear systems in structured and high-order unstructured CFD problems," *Computers & Fluids*, Vol. 244, 2022, p. 105575.

[25] Resmini, A., Peter, J., and Lucor, D., "Mono-block and non-matching multi-block structured mesh adaptation based on aerodynamic functional total derivatives for RANS flow," *International Journal for Numerical Methods in Fluids*, Vol. 83, No. 11, 2017, pp. 866–884.

[26] Méheut, M., Destarac, D., Ben Khelil, S., Carrier, G., Dumont, A., and Peter, J., "Gradient-based single and multi-points aerodynamic optimizations with the elsA software," *53rd AIAA Aerospace Sciences Meeting*, 2015, p. 0263.

[27] Brooks, T. F., and Hodgson, T., "Trailing edge noise prediction from measured surface pressures," *Journal of sound and vibration*, Vol. 78, No. 1, 1981, pp. 69–117.

[28] Jacquin, L., Molton, P., Deck, S., Maury, B., and Soulevant, D., "Experimental study of shock oscillation over a transonic supercritical profile," *AIAA journal*, Vol. 47, No. 9, 2009, pp. 1985–1994.

[29] Finez, A., "Etude expérimentale du bruit de bord de fuite à large bande d'une grille d'aubes linéaire et de sa réduction par dispositifs passifs," Ph.D. thesis, Ecole Centrale de Lyon, 2012.

[30] Koch, R., Sanjosé, M., and Moreau, S., "Acoustic investigation of the transonic RAE 2822 airfoil with large-eddy simulation," *28th AIAA/CEAS Aeroacoustics 2022 Conference*, 2022, p. 2816.